

Dust and molecules in the Local Group galaxy NGC 6822

III. The first-ranked HII region complex Hubble V

F.P. Israel¹, F. Baas^{1,2} †, R.J. Rudy³, E.D. Skillman⁴ and C. E. Woodward⁴

¹ Sterrewacht Leiden, P.O. Box 9513, 2300 RA Leiden, the Netherlands

² Joint Astronomy Centre, 660 N. A'ohoku Pl., Hilo, Hawaii, 96720, USA

³ Space Science Applications Laboratory, M2-266, The Aerospace Corporation, P.O. Box 92957, Los Angeles, California 90009-2957, USA

⁴ Department of Astronomy, University of Minnesota, 116 Church Street SE, Minneapolis, MN 55455, USA

† Deceased April 4, 2001

Received ???; accepted ???

Abstract. We present maps of the first-ranked HII region complex Hubble V in the metal-poor Local Group dwarf galaxy NGC 6822 in the first four transitions of ^{12}CO , the $158\mu\text{m}$ transition of C^+ , the 21-cm line of HI, the Pa β line of HII, and the continuum at 21 cm and $2.2\mu\text{m}$ wavelengths. We have also determined various integrated intensities, notably of HCO^+ and near-IR H_2 emission. Although Hubble X is located in a region of relatively strong HI emission, our mapping failed to reveal any significant CO emission from it. The relatively small CO cloud complex associated with Hubble V is comparable in size to the ionized HII region. The CO clouds are hot ($T_{\text{kin}} = 150\text{ K}$) and have high molecular gas densities ($n(\text{H}_2) \approx 10^4\text{ cm}^{-3}$). Molecular hydrogen probably extends well beyond the CO boundaries. C^+ column densities are more than an order of magnitude higher than those of CO. The total mass of the complex is about $10^6 M_{\odot}$ and molecular gas account for more than half of this. The complex is excited by luminous stars reddened or obscured at visual, but apparent at near-infrared wavelengths. The total embedded stellar mass may account for about 10% of the total mass, and the mass of ionized gas for half of that. Hubble V illustrates that modest star formation efficiencies may be associated with high CO destruction efficiencies in low-metallicity objects. The analysis of the Hubble V photon-dominated region (PDR) confirms in an independent manner the high value of the CO-to- H_2 conversion factor X found earlier, characteristic of starforming low-metallicity regions.

Key words. Galaxies: individual: NGC 6822 – Galaxies: ISM; irregular; Local Group – Radio Lines: ISM; ISM: molecules

1. Introduction

NGC 6822 (DDO 209) is a Local Group dwarf irregular galaxy of the Magellanic type (IB(s)m), located at a distance of 500 kpc (McAlary et al. 1983). Optically, NGC 6822 shows a bar dominated by an irregular distribution of OB associations (Wilson 1992a and references therein) and HII regions (Hodge et al. 1988). At the northern end of the bar, the major HII region complexes Hubble I, III, V and X (Hubble 1925) and several relatively luminous OB associations reside in a ridge of bright neutral hydrogen. The galaxy is embedded in a much more extended envelope of neutral hydrogen (Brandenburg & Skillman 1998; de Blok & Walter 2000).

Maps of the infrared emission from NGC 6822, measured with the IRAS satellite and processed to a resolu-

tion of about $1'$ (145 pc) were presented by Israel et al. 1996a (hereafter Paper I). A $J=1-0$ ^{12}CO survey of NGC 6822 was the subject of Paper II (Israel 1997a). In this paper, the third in the series, we present new observations and maps primarily of the major star formation complex Hubble V but also to some extent of the second major HII region Hubble X. Coordinates (epoche 1950.0) are given in Table 2.

The relatively low metal abundance of its HII regions (Hubble V: $[\text{O}/\text{H}] = 1.6 \times 10^{-4}$; Lequeux et al. 1979; Pagel et al. 1980; Skillman et al. 1989) is consistent with a relatively low time-averaged star formation rate (Paper I). This abundance is about one third that of the Solar Neighbourhood and right between those given by Dufour (1984) for the LMC and the SMC. Also consistent with a relatively low star formation rate is the weak radio continuum emission from NGC 6822 (Klein et al. 1983). The

Table 1. (Sub)mm observations log

Transition	Date (MM/YY)	Freq (GHz)	T_{sys} (K)	η_{mb}
^{12}CO (1–0)	07/96 ^a	115	425	0.70
	07/97 ^a		435	
	06/98 ^b		370	
^{13}CO (1–0)	05/00 ^a	110	330	0.70
	07/96 ^a		235	
^{12}CO (2–1)	07/97 ^a	230	240	0.69
	06/91 ^c		700	
	03/92 ^c		360	
^{12}CO (3–2)	06/98 ^b	345	530	0.45
	07/96 ^c		665	
^{13}CO (3–2)	09/97 ^c	330	2460	0.58
	07/96 ^c		330	
^{12}CO (4–3)	12/94 ^c	461	1280	0.48
	07/98 ^c		3276	
	09/98 ^c		1720	
HCO^+ (1–0)	07/96 ^a	89	125	0.74
	07/97 ^a		120	
CS (3–2)	09/96 ^a	147	160	0.60
$\text{H}_2\text{CO}_{2,2} - 1_{1,1}$	09/97 ^a	141	174	0.60
$\text{H}_2\text{CO}_{2,1} - 1_{1,0}$	09/96 ^a	150	163	0.60
$\text{CI } ^3P_1 - ^3P_0$	12/94 ^c	492	1765	0.43

Notes: ^a SEST 15 m; ^b IRAM 30 m; ^c JCMT 15 m.

galaxy has a dust-to-gas ratio of about 1.4×10^{-4} (Paper I), which is well within the range generally found for dwarf galaxies.

The brightest HII region complex in NGC 6822 is Hubble V, connected to the luminous stars of NGC 6822 OB3 (Wilson 1992a). This association is about 50 pc in diameter, contains 14 OB stars ($M < 20M_{\odot}$) with an estimated total mass of $850M_{\odot}$ and has an age of 6.6 million years (Wilson 1992b) or less (O'Dell et al. 1999). In spite of its optical prominence, Hubble V has a radio luminosity only 15% of that of the first-ranked HII region complex NGC 604 in M 33; it is comparable to bright Galactic HII regions, but would not be counted among the very brightest. Nor is it very luminous in molecular line emission, although it is the brightest discrete source of $J=1-0$ ^{12}CO emission in NGC 6822 (Paper II). Interferometer observations by Wilson (1994) show that about half of the single-dish $J=1-0$ ^{12}CO signal is contributed by compact ($0.1'$) components. Wilson (1994) used this result, assuming virial equilibrium, to derive a CO-to H_2 conversion factor rather similar to that of the Solar Neighbourhood, implying relatively small amounts of H_2 . However, Israel (1997a, b) argued that this conversion factor applies only to the densest molecular clumps in the complex, and derived for the entire complex a conversion factor 20 times higher.

1.1. Molecular line observations

Details relevant to the observations are listed in Table 1. The system temperatures given are the means for the respective runs. Most observations in the 89 - 150 GHz range were obtained with the SEST 15 m telescope at ESO-La Silla (Chile)¹. We used the 100/150 GHz SiS receivers in dual mode, together with the high resolution acousto-optical spectrometer. In split mode, this spectrometer provides two 500 MHz bands with a resolution of 43 kHz. At two positions in Hubble V, ^{12}CO emission was measured in the $J=1-0$ and $J=2-1$ transitions with the IRAM 30 m telescope in Spain.

All other observations were made with the JCMT 15 m telescope on Mauna Kea (Hawaii)². Up to 1993, we used a 2048 channel AOS backend covering a band of 500 MHz. After that year, the DAS digital autocorrelator system was used in a band of 500 and 750 MHz. At 230 GHz, we fully mapped Hubble V in the $J=2-1$ ^{12}CO transition; at 345 GHz and 461 GHz, we made small maps of the $J=3-2$ and $J=4-3$ ^{12}CO transitions covering the emission peak. Resulting spectra were binned to various resolutions in order to obtain the optimum combination of spectral resolution and signal-to-noise ratio. Usually, only linear baseline corrections were applied to the spectra. All spectra were scaled to a main-beam brightness temperature, $T_{\text{mb}} = T_{\text{A}}^*/\eta_{\text{mb}}$; relevant values for η_{mb} are given in Table 1.

In addition to the measurements of Hubble V, we also obtained data on a second and nearby bright HII region complex, Hubble X, and on a prominent infrared continuum/millimeter line source at the southern end of the bar of NGC 6822 (cf. Papers I, II). Even though we mapped the region containing Hubble X proper in $J=1-0$ ^{12}CO , we did not detect a signal above 30% of that from Hubble V. A positive, but noisy result was obtained $1'$ (145 pc) east of Hubble X. Most likely this represents an associated molecular cloud complex.

Spectra are shown in Figs. 1 and 2, and summarized in Table 2. The most remarkable results are (a). the weakness of ^{13}CO with respect to ^{12}CO , and (b). the relatively high intensity of the higher CO transitions with respect to the $J=1-0$ transition. Both suggest a low optical depth for the $J=1-0$ ^{12}CO transition.

The spatial extent of emission in the various ^{12}CO transitions is shown in Figs. 3 and 4. The five-point $J=1-0$ ^{12}CO map at resolution $43''$ (Fig. 3) shows essentially a point source. The $J=2-1$ CO map is peaked at $\Delta\alpha = +5''$, $\Delta\delta = -4''$ with an extension to the northwest. The FWHM size of the CO complex is $29'' \times 25''$, which corresponds to a

¹ The Swedish-ESO Submillimetre Telescope (SEST) is operated jointly by the European Southern Observatory (ESO) and the Swedish Science Research Council (NFR).

² The James Clerk Maxwell Telescope is operated by the Observatories on behalf of the Particle Physics and Astrophysics Council (PPARC) of the United Kingdom, the Netherlands Organization for Scientific Research (NWO), and the National Research Council (NRC) of Canada.

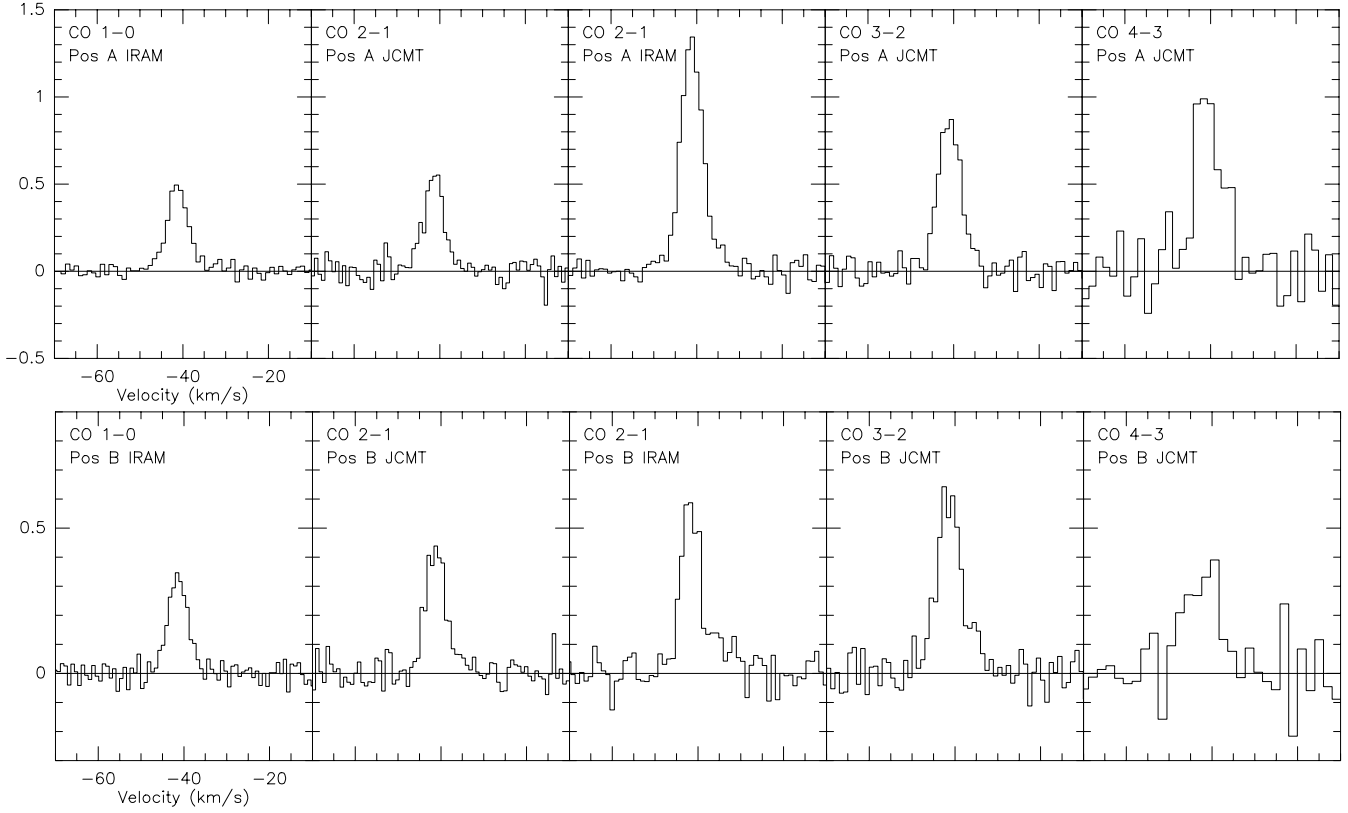


Fig. 1. Hubble V CO profiles of the various transitions. Intensities are given in units of $T_{mb} = T_A^*/\eta_{mb}$; values of η_{mb} used are those listed in Table 1. Velocity scale is V_{LSR} . The spectra in the two leftmost columns were taken at a resolution of about $22''$, the spectra in the three rightmost columns at resolutions of $14'' - 11''$. The spectra at top are those at offset position $\Delta\alpha, \Delta\delta = 0, +2''$; the spectra at bottom are those at offset position $+5'', -4''$; these positions are spatially separated by about $8''$ so that the spectra shown in the two rows are not fully independent.

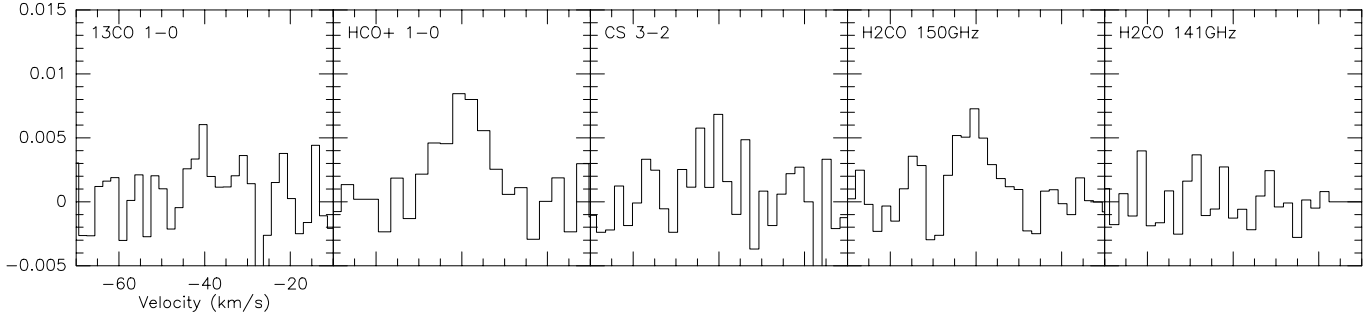


Fig. 2. Hubble V. Other lines observed with SEST; intensities are given in units of $T_A^* = \eta_{mb} \times T_{mb}$; values of η_{mb} are those listed in Table 1. Velocity scale is V_{LSR} .

linear size of 50×35 pc after correction for finite beamsize. Such a small size is consistent with the CO results in the other observed transitions. The $J=3-2$ and $J=4-3$ maps cover most of the emission, but may miss some of the more extended low-surface brightness emission that appears to be present.

We have determined line ratios in identical beams by convolving the higher frequency measurements to the lower frequency beamsizes. The results are given in Table 5 together with typical values for HII regions in the LMC (average of five clouds), the SMC and the starburst core of the dwarf galaxy He 2-10. We also give the line ratios

for the whole Hubble V CO source. Because of the limited extent of our $J = 3-2$ and especially $J = 4-3$ map, we may have somewhat underestimated the integrated emission in these two transitions, so that the ratios given in actual fact could be somewhat higher.

Our single-dish $J=1-0$ and $J=1-0$ CO maps have resolutions of $21''$ and $14''$ respectively, and may thus be compared to the $J=1-0$ CO interferometer map made by Wilson (1994) at a somewhat higher resolution of $6'' \times 11''$. In her interferometer map, Wilson identified three distinct clouds, MC1, MC2 and MC3. The first two appear to form a single complex connected by a bridge. MC3 appears to

Table 2. Emission line intensities

Source	Position $\alpha_o(1950.0)$	$\delta_o(1950.0)$	Offset "	Transition	Beam (")	T_{mb} (mK)	ΔV km s^{-1}	V_{LSR} km s^{-1}	$\int T_{mb}dV$ K km s^{-1}
Hubble V (Pos. A)	19:42:03.2	-14:50:28	0, +2	^{12}CO (1-0)	43	137±12	5.6	-41.3	0.81±0.06
					23	489±31	5.8	-41.2	2.70±0.30
				^{13}CO (1-0)	45	10±7	—	-41	0.035±0.010
				^{12}CO (2-1)	21	545±26	5.5	-41.4	3.18±0.40
					13	1300±70	5.6	-41.2	7.80±0.90
				^{12}CO (3-2)	14	878±56	6.2	-41.0	5.85±0.90
				^{12}CO (4-3)	11	949±59	5.6	-41.4	4.74±0.86
				HCO^+ (1-0)	57	14±3	8	-39.5	0.15±0.025
				CS (3-2)	34	6±4	—	—	0.07±0.03
				H_2CO $2_{1,2} - 1_{1,1}$	35	< 5	—	—	< 0.02
	33	10±4	8	40.7	0.08±0.02				
Hubble V (Pos. B)	19:42:03.2	-14:50:28	+5, -4	^{12}CO (1-0)	23	335±36	5.4	-41.4	1.93±0.21
				^{12}CO (2-1)	21	433±31	5.5	-41.3	2.54±0.30
					13	588±81	5.5	-41.7	3.47±0.35
				^{12}CO (3-2)	14	560±68	6.4	-41.4	3.89±0.55
				^{13}CO (3-2)	14	< 150	—	—	≤ 0.6
				^{12}CO (4-3)	11	354±96	9	-42.1	3.62±0.90
				$\text{Cl } ^3\text{P}_1 - ^3\text{P}_0$	10	< 150	—	—	< 0.9
Hubble X ^a	19:42:15.6	-14:50:31	0, 0	^{12}CO (1-0)	43	< 21	—	—	< 0.25
				^{12}CO (2-1)	21	< 70	—	—	< 0.27
			+59, 0	^{12}CO (1-0)	43	60	10	-32	0.63±0.23
				^{12}CO (2-1)	21	50	8	-36	0.53±0.15
South ^b	19:41:59.0	-14:59:54	0, 0	^{12}CO (1-0)	43	41	21	-50	0.80±0.14
				^{12}CO (2-1)	21	80	18	-44	1.0± 0.25

Notes: ^a. Values for Hubble X represent average result over 3×3 map with $20''$ spacing. ^b. Corresponds to IRS 4/CO cloud 5 (Paper I, II); location of NGC 6822 HI maximum.

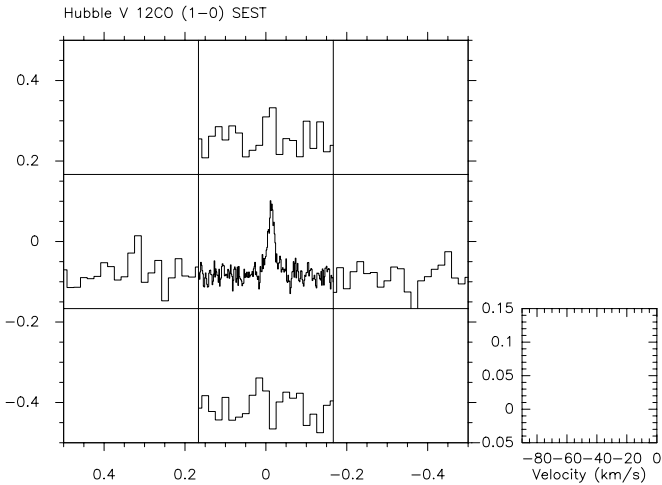


Fig. 3. ^{12}CO $J=1-0$ spectra obtained towards Hubble V at $43''$ resolution. The central profile has a high S/N ratio. The surrounding spectra at SEST-beam halfpower points have much lower S/N ratios and therefore are binned to much lower velocity resolutions. Intensities are in T_A^* . At $43''$ (105 pc) resolution, the CO complex is essentially pointlike.

be a more isolated cloud $30''$ further north; it is outside our maps. The CO emission mapped by us, and shown in Fig. 4, corresponds to Wilson's cloud complex MC1/MC2, although the detailed resemblance is poor. Our $J=3-2$ CO peak is close to MC2, but cloud MC1 and the ridge connecting it to MC2 are not easily recognized in Fig. 4. The implications of this are, however, unclear because the interferometer map suffers from poor U,V plane coverage and strong sidelobe distortion rendering its structural detail uncertain.

1.2. Atomic line observations

JCMT observations of the $^3\text{P}_1 - ^3\text{P}_0$ [CI] transition at 492 GHz, summarized in Table 2, yielded only an upper limit. In Table 3 we give this upper limit expressed in W m^{-2} . The [CII] $158 \mu\text{m}$ observations were made with the MPE/UCB Far-Infrared Imaging Fabry-Perot Interferometer (FIFI; Poglitsch et al. 1991) on the NASA Kuiper Airborne Observatory (KAO) in April 1992. FIFI had a 5×5 focal plane array with detectors spaced by $40''$ (Stacey et al. 1992). Each detector had a FWHM of $55''$ and the beam shape was approximately Gaussian ($68''$ equivalent disk; beam solid angle $\Omega_B = 8.3 \times 10^{-8}$ sr). We observed in 'stare mode' (velocity resolution 50 km s^{-1})

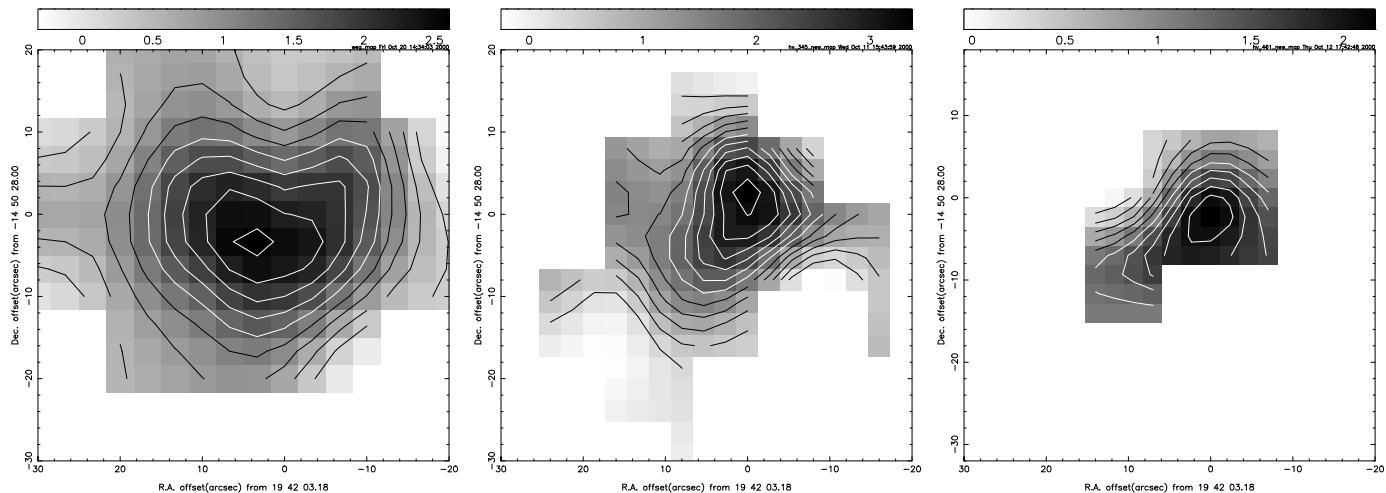


Fig. 4. Contour maps of velocity-integrated emission from Hubble V in NGC 6822 (range: $V_{LSR} = -50$ to -30 km s^{-1}) at full resolution. Left to right: CO $J=2-1$, CO $J=3-2$ and CO $J=4-3$. Contour values are linear in $\int T_{\text{mb}} dV$; steps are 0.4 K km s^{-1} ($2-1$), 0.5 K km s^{-1} ($3-2$) and 0.4 K km s^{-1} ($4-3$). In all maps, north is at top. Because of regridding, actual declination of the $J=4-3$ map differs by $2''$ from the printed scale, and is in fact identical to that of the $J=2-1$ and $J=3-2$ maps.

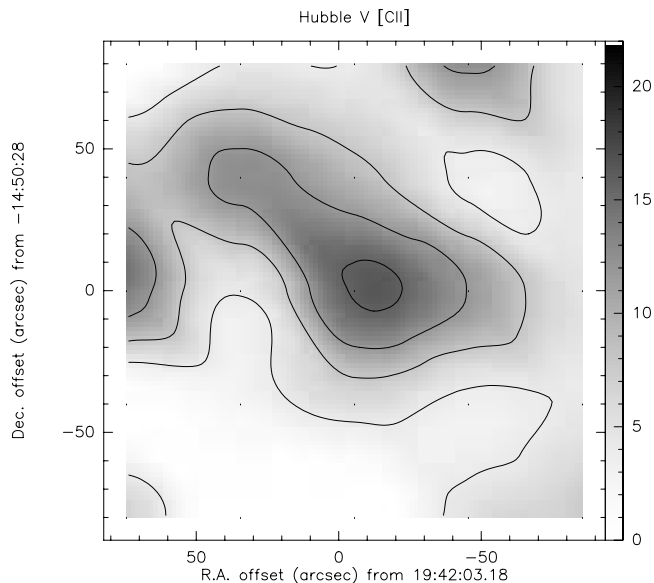


Fig. 5. Map of [CII] emission centered on Hubble V. Contours are linear with both first level and interval of 4×10^{-9} $\text{W m}^{-2} \text{sr}^{-1}$.

by setting the bandpass of the Fabry-Perot to the line center at the object velocity. Observations were chopped at 23 Hz and beam-switched to two reference positions about $6'$ away. The data were calibrated by observing an internal blackbody source. The calibration uncertainty is of the order of 30% and the absolute pointing uncertainty of the array is better than $15''$.

The resulting map is shown in Fig. 5. The [CII] emission is relatively weak. There is a clear peak at the position of Hubble V, and a second peak at $\Delta\alpha = -40''$, $\Delta\delta = +80''$, i.e. 215 pc northwest of Hubble V. A large part of the field is filled by weak and diffuse [CII] emission with a surface

brightness of approximately 8×10^{-9} $\text{W m}^{-2} \text{sr}^{-1}$. The [CII] emission directly associated with Hubble V has a larger extent than the CO emitting region, but the poor [CII] resolution makes it impossible to be more quantitative.

The HI observations of NGC 6822 with the Very Large Array³ consisting of 8 hours (essentially a full transit) in the “D” configuration on 7 September 1992 and another 8 hours in the “CnB” configuration of 5 June 1993 under program AW312 (PI: C. Wilson). The “CnB” configuration was chosen for the higher resolution observations because the galaxy lies at a declination of -14° , resulting in a strongly elliptical synthesized beam for normal configurations. The “D” configuration was chosen for the lower resolution observations in order to maximize the observing time with the Sun below the horizon. The observations were taken at a single pointing (RA = $19^{\text{h}}42^{\text{m}}07^{\text{s}}$, Dec. = $-14^\circ55'42''$, 1950.0), with the correlator in “2AD” mode consisting of 127 channels with widths of 2.5 km s^{-1} (after on-line Hanning smoothing) centered on a heliocentric velocity of -55 km s^{-1} . Total on-source integration time was 383 minutes for the D configuration observations and 340 minutes for the CnB configuration observations. The images were reconstructed with robust weighting resulting in a synthesized beam of $30.3'' \times 16.4''$. Preliminary results were reported in Brandenburg & Skillman (1998), and a more complete report is planned.

The HI distribution shows a local maximum in the atomic hydrogen distribution just north of Hubble V. Emission then extends westwards in a clumpy ridge towards Hubble X. This nebula is likewise located at the edge of a local atomic hydrogen maximum, which is in fact somewhat stronger than the Hubble V maximum.

³ The Very Large Array is a facility of the National Radio Astronomy Observatory

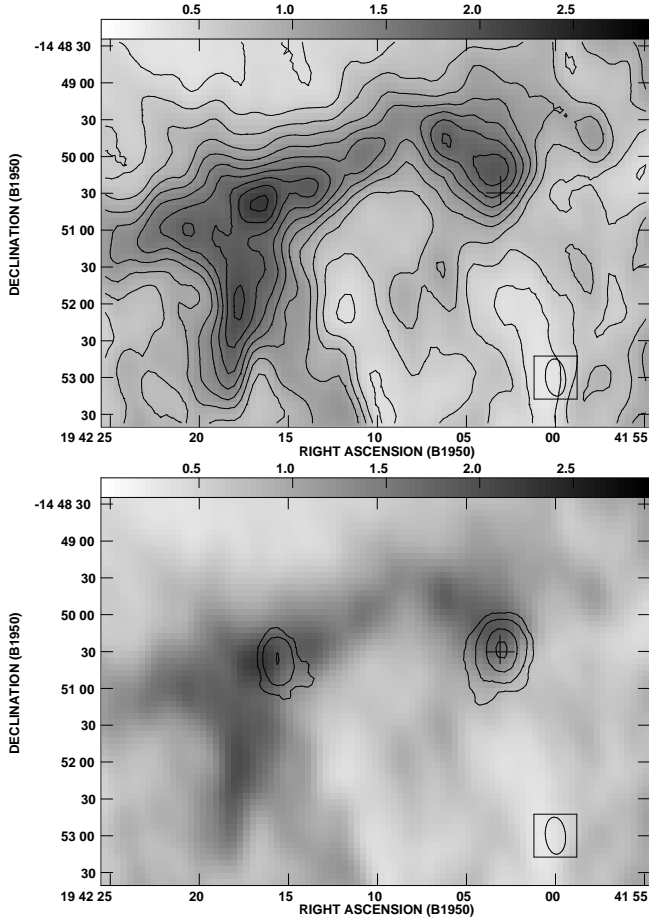


Fig. 6. Comparison of HI 21-cm total column density and 21-cm radio continuum VLA observations of NGC 6822 in the vicinity of Hubble V and Hubble X. Top: map of total HI column density in both greyscale and contour representation. The greyscale is labeled in units of 10^{21} H atoms cm^{-2} with contour levels from 0.2 to 2.2 ascending in increments of 0.2. Bottom: map of radio continuum emission at 21 cm in contour representation plotted on top of the HI column density in greyscale representation (identical to top). The 21-cm radio continuum contours are plotted at values of 1, 2, 5, and 10 mJy/Beam. In both figures, a cross marks the (0,0) position of the CO and [CII] maps; the size of the cross corresponds to $J=2-1$ CO beamsize. The HI synthesized beamsize of $30.3'' \times 16.4''$ is shown by the ellipse in the box in the lower right hand corner.

Although the [CII] and HI distributions are not identical, comparison of Figs. 5 and 6 shows that they follow one another, at least over the region mapped in [CII]. The two HII regions, as traced by their 21-cm continuum emission, are both located close to, but clearly offset from, the ridge of maximum HI intensity. Note that the relative positions of HII and HI are extremely accurate, as they are both derived from the same dataset.

As is the case for HI, [CII] emission likewise extends in a northeast-southwest ridge from Hubble V to Hubble X. In Table 3, we have listed the observed [CII] intensities for the pixel containing Hubble V (Source Peak), for the

extended source of which this pixel is part (Source Total), and for the whole observed field (Field Total).

1.3. Near-infrared hydrogen line and continuum observations

We obtained a near-infrared spectrum, covering the wavelength region from 2.09 to 2.21 μm , in April 1987 with the UK Infrared Telescope (UKIRT), using a single-channel InSb detector equipped with a circular variable filter wheel of constant spectral resolution $\lambda/\Delta\lambda = 120$. The aperture was 19.6'', covering most of the complex. Intensities were calibrated and corrected for atmospheric transmission by observations of the standard stars BS 3903, BS 4550 and BS 6220 ($K = 2.04, 4.39$ and 1.39 mag, and $T_{\text{eff}} = 4800, 5200$ and 4700 K respectively) observed at similar airmass. The $v=1-0$ S(1) H_2 and Brackett- γ lines are clearly detected with equivalent widths of 11 and 34 nm respectively. Line intensities are given in Table 3.

We also used the near-infrared Fabry-Perot imaging spectrometer (FAST; Krabbe et al. 1993) at the Cassegrain focus of the 4.2 m William Herschel Telescope (WHT) at La Palma, Spain, to obtain images of Hubble V in the Br- γ and $v=1-0$ S(1) lines. The FAST camera used an SBRC 58×52 InSb array with a pixel scale of $0.5''$ and a field of about $30'' \times 30''$. A spectral resolution of $\lambda/\Delta\lambda = 950$ was provided by a scanning Fabry-Perot interferometer with a circular variable filter wheel as order-sorter. Images were obtained at the Hubble V central velocity, and at velocities offset from the line by about 300 km s^{-1} . After subtraction of the dark current, the images were flat-fielded and sky-subtracted. The resulting line-plus-continuum images were corrected for atmospheric transmission and instrumental response with the use of the standard stars BS 3888 and BS 4550. As a last step, the mean of the continuum on either side of the line was subtracted from the image containing the line.

Hubble V was detected in Brackett- γ as an amorphous structure of $4'' \times 5''$ FWHM. The integrated flux determined from the map is $1.0 \times 10^{-16} \text{ W m}^{-2}$, uncertain by a factor of two. As the nominal flux is very close to that observed in the 19.6'' aperture of the spectroscopic observations, we take this agreement to indicate that the value in Table 3 is close to the total Brackett- γ line intensity of Hubble V. The H_2 image did not yield a detection. The r.m.s. noise in the map is $2 \times 10^{-8} \text{ W m}^{-2} \text{ sr}^{-1}$. The two- σ upper limit to the surface brightness and the line flux given in Table 3 then suggest that the H_2 emission is relatively smooth and extended on a scale larger than $6''$. For comparison purposes, we have also listed the $\text{H}\alpha$ flux integrated over the whole HII region complex determined by Hodge et al. (1989). According to Fig. 1 of Hodge et al. (1989), our 19.6'' (48 pc) aperture should contain about 70% of the total Brackett- γ flux.

Finally, Hubble V was observed in August 1998, in J, H and K_s broadband filters, as well as in narrow-band filters centered on the wavelengths of the Pa β and (1-0)

Table 3. Hubble V. Carbon and hydrogen line emission

Transition	Resol. (")	F_{line} (W m^{-2})	Remarks
CI $^3\text{P}_1 - ^3\text{P}_0$	10	<7.4 (-19)	
CII $J = \frac{3}{2} - \frac{1}{2}^2\text{P}$	55	1.6±0.2 (-15)	Source Peak
		2.8±0.4 (-15)	Source Total
		6.9±0.9 (-15)	Field Total
H ₂ $v=1-0$ S(1)	19.6	2.8±0.7 (-17)	
HII Br γ^a	19.6	8.4±1.0 (-17)	
HII Pa β	—	4.2±1.0 (-16)	Bright Only
HII H α^b	—	4.8±0.5 (-15)	Source Total
FIR	—	4.7±1.2 (-13)	Paper I

Notes: ^a. Corresponding to about 70% of source total (see text)

^b. O'Dell et al. (1999)

Table 4. Hubble V. Near-infrared photometry

Object	K_s	$H - K_s$ (mag)	$J - H$	Type
North	14.52	+0.06	+0.55	Foreground Star
Center	15.35	+0.16	+0.67	Visible Cluster
South	15.93	≥ 1.07	—	Obscured Cluster

S(1) H₂ lines. The K_s bandpass is an abbreviated version of the standard K -band filter, spanning the wavelength range from 1.98 to 2.32 μm , chosen to minimize the thermal background. The near-infrared images were acquired with the Aerospace Corp. near-infrared camera. This is a liquid nitrogen cooled imager based on the NICMOS3 detector. When configured for use at the Wyoming Infrared Observatory the camera has a 110 x 110 arcsecond field of view. A more detailed description is provided by Rudy et al. (1997). The standard star employed for the August 1998 images was HD 225023 whose near-infrared magnitudes are tabulated by Elias (1982). The Pa β images were acquired using a narrow passband filter (FWHM = 122 angstroms); the Pa β flux was calculated by using the J-band image to estimate and remove the continuum emission. The full extent of Pa β emission is about 6", and the nebula shows little structural detail.

2. Analysis

2.1. Hubble V foreground extinction

Assuming intrinsic line ratios $\text{H}\alpha/\text{Pa}\beta = 17.4$ and $\text{H}\alpha/\text{Br}\gamma = 104.4$ (Pengelly, 1964; Giles 1977), our line fluxes (Table 3) predict the source-averaged reddening to be $0.35 < E(B - V) < 0.55$ mag with a total dereddened flux $S(\text{H}\alpha) = 1.2 \pm 0.2 \times 10^{-14} \text{ W m}^{-2}$. This reddening is higher than the (mostly Galactic foreground) reddening $E(B - V) = 0.24 - 0.36$ mag (Gallart et al. 1996; Massey

et al. 1995; McAlary et al. 1985). Although our value is comparable to the median reddening of early type stars in NGC 6822 ($E(B - V) = 0.45$ mag (Wilson 1992b; Bianchi et al. 2001), it must be considered a lower limit, because neither the Pa β nor the Br γ fluxes represent all the flux of Hubble V sampled in H α .

With flux-densities $S_{1.5\text{GHz}} = 20$ mJy, $S_{4.8\text{GHz}} = 17$ mJy and $S_{10.7\text{GHz}} = 16$ mJy (Condon 1987; Klein & Gräve 1986; Klein et al. 1983) the radio continuum emission from Hubble V (Fig. 6) is clearly thermal and optically thin. From these radio continuum flux-densities and the H α flux we obtain for $T_e = 11\,500$ K (Lequeux et al. 1979; Skillman et al. 1989) a more accurate *overall* reddening $E(B - V) = 0.65$ mag. Thus, the nebula appears to suffer a higher mean reddening than NGC 6822 as a whole. This agrees, at least qualitatively, with the finding that in the Magellanic Clouds the younger stellar population suffers significantly more reddening than the older population (Zaritsky 1999; Zaritsky et al. 2002). However, in the next section we will show that in actual fact much of the nebula is only modestly reddened, whereas a part is almost completely obscured at visual wavelengths, and becomes progressively more visible at near-infrared wavelengths only.

2.2. The Hubble V radiation field

The H α map by Collier & Hodge (1994) exhibits a typical core-halo structure. More detail is supplied by an HST image of Hubble V, based on data procured and discussed by O'Dell et al. (1999) and Bianchi et al. (2001). This image (Fig. 7) shows the core to contain a cluster of luminous stars, and the halo to consist of diffuse and filamentary structures against which several OB association member stars can be seen (cf. Bianchi et al. 2001). Most relevant to us are the clear indications of substantial obscuration in the northeastern and especially southeastern part of the complex. The core appears to be the region directly in contact with the molecular cloud complex, whereas the halo is mostly ionized gas expanding into surrounding space (cf. O'Dell et al, 1999). The individually identified early type stars (see e.g. Massey et al. 1995) are all in the relatively diffuse western halo part of the nebula. The excitation parameter of an HII region complex is defined as $u = 14.2(S_{4.8}D^2T_e^{0.35})^{1/3}$ with flux-density S_ν in Jy, distance D in kpc, and T_e in 10^4 K (cf. Mezger & Henderson 1967). Using the radio flux-densities from the previous section, we find for the Hubble V HII region complex $u = 234 \text{ pc cm}^{-2}$. This implies a *minimum* Lyman continuum photon flux $N_L = 8.45 \times 10^{50} \text{ photons s}^{-1}$ (Panagia 1973), corresponding to the UV output of more than a dozen O5 stars. From the compilation by Wilson (1992a) we may estimate that previously identified early-type stars can contribute, at face value, no more than about three quarters of this *minimum* required Lyman continuum flux. Moreover, as the HII region appears to be partly density-bounded, the actually required flux should be higher by more than

Table 5. Hubble V. Normalized line intensities

Transition	Resol.		Normalized Intensity					
	($''$)	Pos. A.	Hubble V Pos. B	Total	LMC ^a		SMC ^b LIRS 36	He 2-10 ^c
¹² CO (1-0)	43	—	—	0.6±0.1	0.95	0.9	0.8	1.0
	21	0.9±0.1	0.8±0.1	—	—	—	—	—
¹² CO (2-1)	—	1	1	1	1	1	1	1
¹³ CO (2-1)	21	—	—	—	0.15	0.14	0.13	0.05
¹² CO (3-2)	14	0.9±0.2	1.1±0.1	1.2±0.2	1.6	0.9	0.9	1.3
¹² CO (4-3)	14	0.5±0.1	1.0±0.1	0.7±0.1	—	—	—	—
¹³ CO (3-2)	14	—	≤0.16	—	—	—	—	0.08
CI ³ P ₁ – ³ P ₀	14	—	<0.25	—	—	—	—	—
CII $J = \frac{3}{2} - \frac{1}{2}$ P	55	—	—	13±5	25	5	10	—
¹² CO (1-0)	—	—	—	1	1	1	1	1
¹³ CO (1-0)	43	—	—	0.043±0.012	0.09	0.10	0.11	<0.05
HCO ⁺ (1-0)	57	—	—	0.31±0.06	0.29	0.14	0.07	—
CS (3-2)	34	—	—	0.06±0.03	0.03	0.03	0.02	—
H ₂ CO	35	—	—	0.07±0.03	0.04	0.03	0.02	—

Notes: a. LMC data: Johansson et al. (1994); Israel et al. (1996a); Chin et al. (1997); Heikkilä et al. (1999). b. SMC data: Chin et al. (1998); Israel (unpublished); c. Baas et al. 1994.

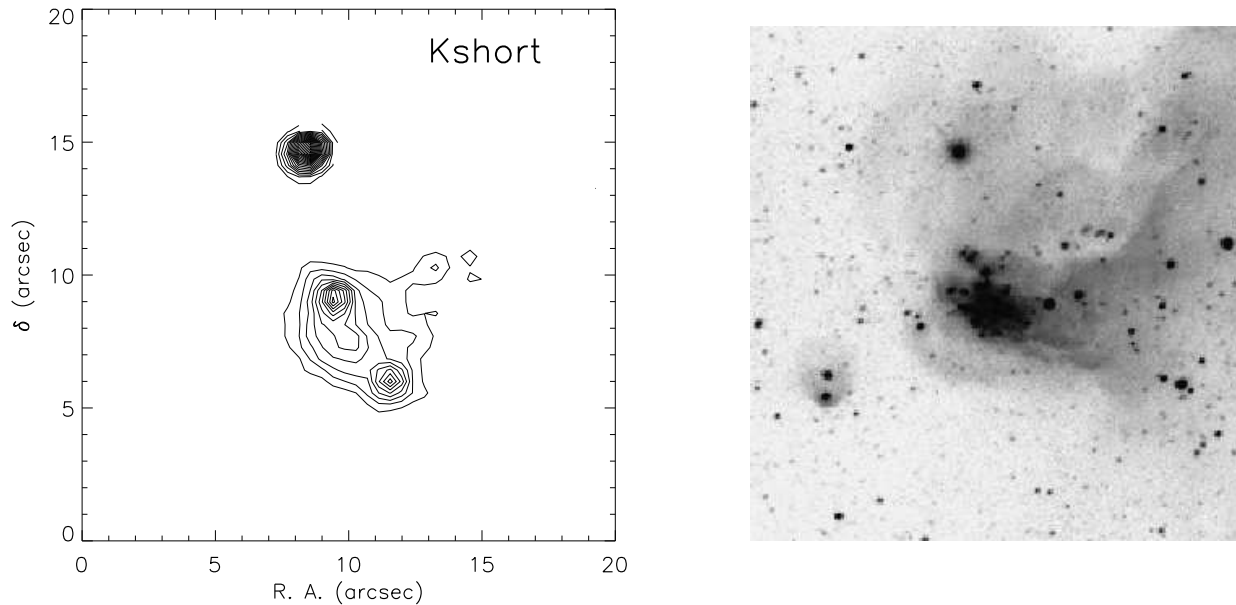


Fig. 7. Left: Near-infrared K-band image of Hubble V and its surroundings. As no absolute position is available, only offsets relative to a randomly chosen position are supplied. Right: Corresponding part of the NASA/ESA/STScI HST image based on data from O’Dell et al (1999) and Bianchi et al. (2001). The northern Galactic foreground star and the stellar cluster in Hubble V, easily seen in both images, were used to bring the HST image and the K-band image to the same scale and line-up. The southern K_s band object, presumably representing an embedded cluster, has no visual counterpart. Most of the extended nebular emission apparent in the near-IR image is likewise heavily obscured. Full-color HST image may be found on the web at <http://heritage.stsci.edu/2001/39/>

a factor of two, thus relegating the role of the identified stars to that of minor contributors. Moreover, these estimates assume that the identified stars are *embedded* in the nebula. As the HST image shows that many of these stars may be detached from the nebula, this is *not* the case, and

their contribution to the *actual* excitation of Hubble V is even less, and probably quite minor if not negligible.

Our K_s -band image of Hubble V and its surroundings (Fig. 7) shows three unresolved objects, as well as nebular emission (primarily $\text{Br}\gamma$) extending into the southeastern obscuration. The HST image and the infrared measure-

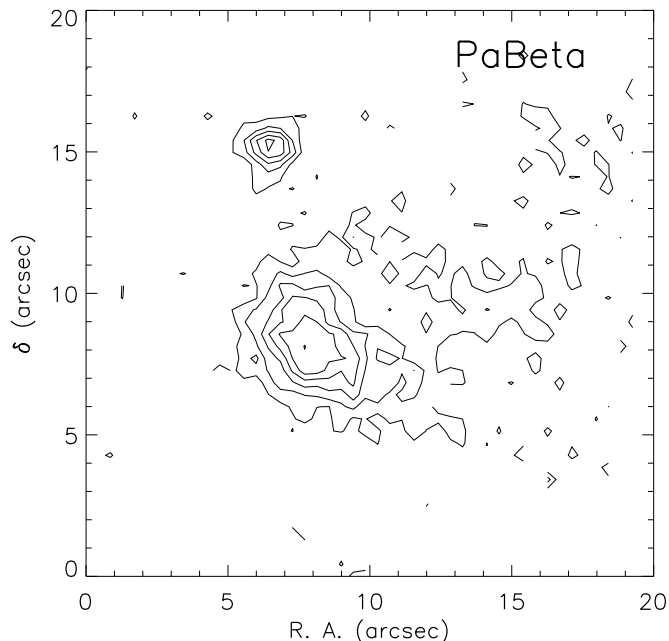


Fig. 8. Near-infrared Paschen- β line image of Hubble V and its surroundings. Again only offsets relative to a randomly chosen position are supplied. Contours are linear in multiples of the lowest contour; contour step is 16.98 mag per square arcsecond corresponding to $4.5 \times 10^{-18} \text{ W m}^{-2} \text{ arcsec}^{-2}$. The bright core, presumably containing ionization fronts, is well depicted; the more diffuse extended emission to the north and west is more poorly represented. The unresolved object north of the nebula is a residual continuum emission from an imperfectly subtracted bright foreground star - see Fig. 7.

ments summarized in Table 4 suggest that the northernmost object is a relatively unreddened star of late spectral type in the Milky Way foreground. The central object ($K_s = 15.35 \text{ mag}$) coincides with a cluster of stars in the HST image (Fig. 7). The infrared colours suggest that the emission is dominated by light from K (super)giants, again with relatively little reddening. However, the southernmost object has no optical counterpart and instead coincides with a region of high obscuration in the HST image. It is not even seen in the J and H bands ($H \geq 17.0 \text{ mag}$ and $J \geq 17.6 \text{ mag}$), indicating an extinction at K of the order of 1.5 mag, i.e. $A_V \geq 17 \text{ mag}$ ($E(B - V) \geq 5.4 \text{ mag}$). Most likely, it represents a cluster of luminous stars responsible for a significant part, if not all, of the excitation of Hubble V and the heating of the molecular cloud observed by us.

In (Fig. 8) we show the nebula imaged in the $\text{Pa}\beta$ line. Comparison of the distribution of line emission with respect to the (northern) foreground star show that it is brightest between the central and southern clusters, i.e. likewise in a region obscured at visual wavelengths. The nebular complex radius is about 20 pc. Taking the HII region-derived Lyman flux and assuming this to originate in a point source separated by 20 pc from the HII

region/neutral cloud interface represented by the bright core, we find the strength of the UV radiation field at the interface to be $I_{\text{UV}} = 725$. Here, the unit chosen is such that $I_{\text{UV}} = 1$ corresponds to a flux $I_{1000} = 4.5 \times 10^{-8} \text{ photons s}^{-1} \text{ cm}^{-2} \text{ Hz}^{-1}$ (Black & van Dishoeck 1987). Alternatively, we may express the strength of the radiation field as $G_o \approx 300$, in units of $12.6 \times 10^{-6} \text{ W m}^{-2}$. This makes Hubble V similar to the LMC HII regions N 159 and N 160 (see Israel et al. 1996b; Bolatto et al. 2000).

2.3. The Hubble V PDR

The characteristics of the Hubble V environment (strong local radiation fields, low metallicity and relatively little radiation shielding) are typically those of a strongly photon-dominated region (PDR). The data collected in this paper provide good diagnostics for the PDR properties of Hubble V. The observed ratios $\log I([\text{CII}])/I(\text{FIR}) = -2.5$ and $\log I(\text{CO J}=1-0)/I(\text{FIR}) = -6.8$ can be used as analytical tools in the PDR models calculated by Kaufman et al. (1999 - notably their Figs. 17 and 1). These ratios apply to low-metallicity surroundings suffering moderate slab extinctions $A_V \approx 3$, radiation fields $G_o = 100 - 300$ and high densities $N_o \approx 10^4$; $n_{\text{CII}} \leq n_{\text{CO}}$. Kinetic temperatures should be of the order of $T_{\text{kin}} \approx 150 \text{ K}$.

Further details are provided by radiative transfer models (Jansen 1995; Jansen et al. 1994) which yield model CO line intensities as a function of gas kinetic temperature, H_2 density and CO column density per unit velocity. These model line intensities are coupled to actually observed values by a further parameter, the beam filling factor f_{CO} . Thus, the four free parameters are essentially constrained by the four observed ^{12}CO transitions. Additional weak constraints are provided by the ^{13}CO measurements. However, the line ratios are not uniquely diagnostic for the possible combinations of input parameters. For instance, non-identical but nevertheless very similar line ratios are produced by simultaneously reducing H_2 density and increasing kinetic temperature, with only little tweaking of CO column densities required. As the actual measurements suffer from finite (and not very small) errors, they do not yield unique solutions.

It turns out that the line ratios of the positions A and B listed in Table 5 each yield two different solutions: a gas of relatively low temperature $T_{\text{kin}} = 30 \text{ K}$ but with high densities $n(\text{H}_2) = 10^4 - 10^5$, or a significantly hotter gas $T_{\text{kin}} = 100 - 150 \text{ K}$ of lower density $n(\text{H}_2) = 3 \times 10^3 - 10^4$. As shown at the beginning of this section, the latter solutions must be preferred in view of the relative intensities of CO, [CII] and FIR emission. The line ratios for positions A and B could be fitted with a single gas component, but this is not possible for the integrated emission of Hubble V. If we assume that the ratios listed in Table 5 are actually lower limits, the severity of this problem only increases.

Accordingly, we have modelled this emission with two separate components. Because the consequent doubling of free parameters brings their number to a total of eight,

Table 6. Hubble V. Model parameters

Pos.	Component 1				Component 2				Line Ratios ^a					
	T_k (K)	$n(\text{H}_2)$ (cm^{-3})	$\frac{N(\text{CO})}{dV}$ ($\frac{\text{cm}^{-2}}{\text{km s}^{-1}}$)	Weight	T_k (K)	$n(\text{H}_2)$ (cm^{-3})	$\frac{N(\text{CO})}{dV}$ ($\frac{\text{cm}^{-2}}{\text{km s}^{-1}}$)	Weight	R_{12}	R_{32}	R_{42}	R_1	R_2	R_3
A	150	3000	6×10^{16}	1.0	—	—	—	—	0.9	0.8	0.6	43	21	21
B	150	10000	3×10^{17}	1.0	—	—	—	—	0.7	1.0	0.9	35	13	9
Total	150	10000	1×10^{16}	0.7	150	1000	3×10^{16}	0.3	0.6	1.1	0.8	41	38	42
Total	150	10000	6×10^{15}	0.6	150	500	1×10^{16}	0.4	0.6	1.1	0.8	45	49	40

Notes: a. Line Ratios: $R_{i2} = {}^{12}\text{CO}(J=i-i-1)/{}^{12}\text{CO}(J=2-1)$; $R_j = {}^{12}\text{CO}/{}^{13}\text{CO}(J=j-j-1)$; values of R_j are calculated for a ${}^{12}\text{CO}/{}^{13}\text{CO}$ abundance ratio of 60. Because of low optical depths, R_j values scale linearly with assumed abundance ratio

in excess of the number of independent measurements, this will always yield a set of non-unique solutions. As before, we reject low temperature/high density solutions, thus reducing the range of possible solutions. We find the hottest and densest component to be tightly constrained by the observations, with $T_{\text{kin}} = 150$ K, $n(\text{H}_2) = 10^4 \text{ cm}^{-3}$ and $N(\text{CO})/dV = 0.6\text{--}1.0 \times 10^{16} \text{ cm}^{-2}$. However, the more tenuous component is only weakly constrained: in principle, H_2 densities can be anywhere between 500 cm^{-3} and 3000 cm^{-3} , kinetic temperatures are anywhere between 150 K (for the lower densities) and 20 K (for the higher densities). We have therefore further reduced the range of possible solutions by retaining only those cases where the more tenuous component is not cooler than the denser component, as we consider this to be physically more plausible than the reverse. We have listed the the resulting representative model solutions in Table 6. It is important to note that more accurate determination of ${}^{12}\text{CO}$ intensities would not greatly improve the situation as the various model-predicted line ratios are virtually identical. Better determination of ${}^{13}\text{CO}$ intensities would help, but only if it were done very accurately as even here differences between the various solutions are not very great (see Table 6).

2.4. Excited H_2 and other molecular species

Emission by H_2 has been detected in its (1–0) S(1) transition with a very low surface brightness of $4 \times 10^{-6} \text{ erg s}^{-1} \text{ cm}^{-2} \text{ sr}^{-1}$ averaged over a relatively large aperture of $19.6''$. However, the lack of a detection in the H_2 image at arcsec resolutions (Sect. 2.3) above a level of $4 \times 10^{-5} \text{ erg s}^{-1} \text{ cm}^{-2} \text{ sr}^{-1}$ suggests that this H_2 emission is relatively widespread, and does not contain high-contrast structure. This, in turn, suggests that the H_2 emission is dominated by UV rather than by shock excitation as is the case for HII regions in the Magellanic Clouds (Israel & Koornneef 1991). The values for Hubble V are also quite reminiscent of those pertaining to NGC 604, the much brighter first-ranked HII region in M 33. Towards that complex, Israel et al. (1989) measured emission from radiatively excited (fluorescent) H_2 with an (almost identical) mean surface brightness.

In Table 5 we have also compared the millimeter and submillimeter line ratios determined for Hubble V with those found for sources in the Magellanic Clouds and the starburst galaxy He 2-10. Generally, Hubble V appears to be hotter than most sources in the LMC and the SMC, and to suffer more from CO photo-dissociation. The line ratios for the fairly extreme 30 Doradus PDR and the starburst core of He 2-10 come closest to those of Hubble V. It is of particular interest to note that in Hubble V, the $J=1-0$ HCO^+ line is much stronger than the $J=1-0$ ${}^{13}\text{CO}$ line (see Fig. 2) as usually the reverse is the case. If we assume HCO^+ to be at the same high temperature $T_{\text{kin}} = 150$ K as the CO, we obtain an HCO^+/CO abundance of 10^{-3} , which is much higher than found for the Magellanic regions (Chin et al. 1997, 1998; Heikkilä et al. 1999). Because CO suffers from relatively intense photo-destruction, the HCO^+ overabundance is less extreme when related to H_2 . In any case, the relatively high intensity of HCO^+ emission is in line with conclusions by Johansson et al. (1994) and Heikkilä et al. (1999) that this line is enhanced in active star formation regions. The possible detections of the CS $J=3-2$ and $\text{H}_2\text{CO } 2_{1,1}-1_{1,0}$ transitions are so marginal that no useful conclusions can be based on them.

2.5. Mass of the Hubble V complex

The amount of carbon monoxide associated with Hubble V is not very large. First, the emission has a low optical depth. In fact, the high-density component in the last two rows of Table 6 is optically thin in all four transitions observed. Second, its surface filling factor is low. For the total source, surface filling factors are of order 0.3 and 0.17 for the dense and tenuous components respectively. Third, the extent of CO emission is small, so that e.g. the $J=1-0$ ${}^{12}\text{CO}$ measurements suffer also from beam dilution as the $43''$ beam is larger than the CO source.

Although the peak of the [CII] emission coincides, within the limits imposed by a limited resolution, with the HII/CO complex, this emission extends well beyond the boundaries of the complex and follows the HI distribution (Figs. 5, 6). Because the HI column density towards Hubble V and its surroundings is of order $N(\text{HI}) \approx 1 - 2 \times 10^{21} \text{ cm}^{-2}$, it is likely that the extent of molecular hydrogen also significantly exceeds that of CO. In partic-

ular at the high radiation field intensities characterizing Hubble V, the expected (Kaufman et al. 1999) and observed intensities imply an overall dilution of the [CII] emission due to incomplete surface and beam filling by a factor of 5 to 10. From the radiative transfer models, we find that in Hubble V, C^+ column densities on average exceed those of CO by a large factor of 20 ± 10 . Indeed, the ratio $F_{CII}/F_{CO} = 3 \pm 1 \times 10^4$ is identical to the high ratio that Israel et al. (1996b) found in the LMC complex N 160 which they considered to be in an advanced stage of CO destruction.

If we neglect possible contributions by C^o , the models provide total carbon column densities which can be converted to total hydrogen column densities, provided the $[C]/[H]$ abundance is known. This has not yet been measured for Hubble V, but we may use the data collected by Garnett et al. (1999, notably their Fig. 4) to estimate $[C]/[H]$ from the known oxygen abundance $[O]/[H]$. If we furthermore estimate that in relatively cool molecular environments about 70% of all carbon will be locked up in dust grains (i.e. the depletion factor $\delta_C = 0.3$), we find a gas-phase abundance ratio $\delta_C \times [C]/[H] \approx 1.8 \times 10^{-5}$. From this, we find for the Hubble V complex a molecular mass $M(H_2) = (6 \pm 3) \times 10^5 M_\odot$ and a total gas mass, including HI and He, of $M_{gas} = (10 \pm 5) \times 10^5 M_\odot$.

These masses are an order of magnitude greater than the *upper limit* to the ionized hydrogen mass $M(HII) \leq 7 \times 10^4 M_\odot$ derived from the radio flux-densities in Sect. 2.1 under the assumption of a homogeneous gas distribution (cf. Mezger & Henderson 1967) and also much larger than the total mass $M(O) \approx 2 \times 10^3 M_\odot$ estimated by Wilson (1992a) contained in stars with mass greater than $15 M_\odot$ (i.e. earlier than spectral type B0). In Sect. 3.2 we surmised that a similar number of stars may have escaped attention by having high extinctions. Moreover, if the stellar ensemble associated with Hubble V is associated with a Miller-Scalo (1979) initial mass function, nonionizing stars may increase the total stellar mass by a factor of about 20. Thus, the total mass of all embedded stars will be of the order of $10^5 M_\odot$, i.e. an order of magnitude less than the total neutral gas mass.

The molecular results imply a CO-to- H_2 conversion factor of $X = 54 \pm 27 \times 10^{20} \text{ cm}^{-2} (\text{K km s}^{-1})^{-1}$. The fact that this result is *identical* to that obtained in Paper II is no doubt fortuitous. This independently derived result does confirm, however, the high value of the X -factor calculated there.

3. Conclusions

1. We have presented maps of the ^{12}CO emission in four transitions associated with the extragalactic HII region complex Hubble V. The extent of the CO emission is rather limited, and comparable to the extent of the ionized gas forming the HII region.
2. We have also measured the integrated emission from the complex in transitions of HCO^+ and marginally detected $J=1-0$ ^{13}CO , $J=3-2$ CS and H_2CO . The

complex and its surroundings were mapped in C^+ . The resulting various line ratios show that most CO in Hubble V is optically thin in at least the lower observed transitions.

3. The Hubble V complex has all the characteristics of a relatively extreme photon-dominated region (PDR), in which a severely eroded CO core exists in a significantly larger cloud of H_2 and HI. In such an extreme PDR, cloud parameters appear better represented by the properties of the dissociation product carbon, traced by [CII] emission, than by the remnant CO.
4. The average reddening of the HII region and the visible OB associations is $E(B - V) = 0.50-0.65$ mag. However, the molecular cloud obscures most of the stars responsible for the excitation of Hubble V at optical wavelengths although they can be seen in the near-IR K -band.
5. Comparison of the observations to chemical and radiative transfer models indicates that the CO occurs in high-density (typically $n(\text{H}_2) = 10^4 \text{ cm}^{-3}$) parts of the molecular cloud complex at high temperatures ($T_{\text{kin}} \approx 150$ K). Although the space density of molecular gas containing C^+ may be lower than that traced by CO emission, the former has much higher column densities.
6. The mass of the whole complex is of the order of $10^6 M_\odot$. Slightly less than two thirds of this mass is in the form of molecular gas, and the remainder is mostly neutral atomic gas. The ionized gas and the embedded stars account for typically 15% of the total mass. The CO molecule is rather efficiently destroyed in Hubble V, even though the efficiency of star formation is not particularly high.
7. The weakness of CO emission, and its small spatial extent do not imply a similar paucity of H_2 gas. The relatively low metallicity of Hubble V provides insufficient shielding for CO in most of the complex; the strongly selfshielding H_2 is only little affected by strong but not extremely intense radiation fields. As a consequence, Hubble V is characterized by a rather high CO-to- H_2 conversion factor $X \approx 5 \times 10^{21} \text{ cm}^{-2} \text{ km s}^{-1}$, as indeed surmised earlier.

Acknowledgements. It is a pleasure to thank the operating personnel of the SEST and the JCMT for their support, and Ute Lisenfeld for conducting the IRAM 30 m service observations. The [CII] measurement was obtained in a program of measuring various Magellanic Cloud HII regions, involving also Phil Maloney, Gordon Stacey, Sue Madden and Albrecht Poglitsch. Some of the near-infrared observations of H_2 and $\text{Br}\gamma$ were likewise obtained within the framework of a different observing program with Paul van der Werf. Bob O'Dell and Luciana Bianchi kindly permitted use of the NASA/ESA/STScI HST image of Hubble V based on their data. RJR was supported by the Independent Research and Development program at The Aerospace Corporation.

References

- Baas F., Israel F.P., & Koornneef J., 1994, *ApJ* 284, 403
- Bianchi L., Scuderi S., Massey P., & Romaniello M., 2110 *AJ* 121, 2020
- Black J.H., & van Dishoeck E.F., 1987, *ApJ* 322, 412
- Bolatto A.D., Jackson J.M., Israel F.P., Zhang X., & Kim S., 2000, *ApJ* 545, 234
- Brandenburg H.J., Skillman E.D., 1998, *BAAS*, 30, 1354
- Chin Y.-N., Henkel C., Whiteoak J.B., et al., 1997, *A&A* 317, 548
- Chin Y.-N., Henkel C., Millar T.J., Whiteoak J.B., & Marx-Zimmer M., 1998, *A&A* 330, 901
- Collier J., & Hodge P., 1994, *ApJS* 92, 119
- Condon J.J., 1987, *ApJS* 65, 485
- de Blok W.J.G., & Walter F., 2000, *ApJL* 537, L95
- Dufour R.J., 1984, in *Structure and Evolution of the Magellanic Clouds*, IAU Symp. 108, Eds. S. van den Bergh and K.S. de Boer (Dordrecht: Kluwer), p. 353
- Elias J. H., Frogel J. A., Matthews K., & Neugebauer G., 1982, *AJ* 87, 1029
- Gallart C., Aparicio A., & Vilchez J.M., 1996, *AJ* 112, 1928
- Garnett D.R., Shields G.A., Peimbert M., et al. 1999, *ApJ* 513, 168
- Giles K, 1977, *MNRAS* 180, 57P
- Heikkilä A., Johansson L.E.B., & Olofsson H., 1999, *A&A* 344, 817
- Hodge P.W., Kennicutt R.C., & Lee M.G., 1988, *PASP* 100, 917
- Hodge P.W., Kennicutt R.C., & Lee M.G., 1989, *PASP* 101, 32
- Hubble E., 1925, *ApJ* 62, 409
- Israel F.P., & Koornneef J., 1991, *A&A* 250, 475
- Israel F.P., Hawarden T.G., Wade R., Geballe T.R., & van Dishoeck E.F., 1989, *MNRAS* 236, 89
- Israel F.P., Bontekoe Tj. R., & Kester D.J.M., 1996a, *A&A* 308, 723 (Paper I)
- Israel F.P., Maloney P.R., Geis N., et al. 1996b, *ApJ* 465, 738
- Israel F.P. 1997a, *A&A* 317, 65 (Paper II)
- Israel F.P. 1997b, *A&A* 328, 471
- Jansen D.J., 1995, Ph.D. thesis, Leiden University (NL)
- Jansen D.J., van Dishoeck E.F., & Black J.H., 1994, *A&A* 282, 605
- Johansson L.E.B., Olofsson H., Hjalmarsen A., Gredel R., & Black J.H., 1994, *A&A* 291, 89
- Kaufman M.J., Wolfire M.G., Hollenbach D.J., & Luhman M.L., 1999, *ApJ* 527, 795
- Klein U., Gräve R., & Wielebinski R., 1983, *A&A* 117, 332
- Klein U., & Gräve R., 1986, *A&A* 161, 155
- Krabbe A., Rotaciuc V., Storey J.W.V., et al 1993, *PASP* 105, 1472
- Lequeux J., Peimbert M., Rayo J.F., Serrano A., & Torres-Peimbert S., 1979, *A&A* 80, 155
- McAlary C.W., Madore B.F., McGonegal R., McLaren R.A., & Welch D.L., 1983, *ApJ* 273, 539
- Massey P., Armandroff T.E., Pyke R., Patel K., & Wilson C.D., 1995, *AJ* 110, 2715
- Mezger P.G., & Henderson A.P., 1967 *ApJ* 147, 471
- Miller G.E., & Scalo J.M., 1979 *ApJS* 41, 513
- O'Dell C.R., Hodge P.W., & Kennicutt R.C., 1999, *PASP* 111, 1382
- Panagia N, 1973, *AJ* 78, 929
- Pagel B.E.J., Edmunds M.G., & Smith G., 1980, *MNRAS* 193, 219
- Pengelly R.M., 1964, *MNRAS* 127, 518
- Poglitsch et al., 1991, *Int. J. Infrared Millimeter Waves* 12, 1589
- Rudy R. J., Woodward C. E., Hodge T., Fairfield S. W., & Harker D. E., 1997, *Nature* 387, 159
- Skillman E.D., Terlevich R., & Melnick J., 1989, *MNRAS* 240, 563
- Stacey G.J., Beeman J.W., Haller E.E., et al., 1992, *Int. J. Infrared Millimeter Waves* 13, 1689
- Wilson C.D., 1992a, *AJ* 104, 1374
- Wilson C.D., 1992b, *ApJL* 384, L29
- Wilson C.D., 1994, *ApJL* 434, L11
- Zaritsky D., 1999 *AJ* 118, 2824
- Zaritsky D., Harris J., Thompson I.B., Grebel E.K. & Massey P., 2002 *AJ* 123, 855